Available online at www.sciencedirect.com

ScienceDirect

IFAC PapersOnline CONFERENCE PAPER ARCHIVE

IFAC PapersOnLine 55-37 (2022) 113–118

Noise Rejection Mode Imaging of Atomic Force Microscope

Jiarong Chen * **Qingze Zou** **

* *Department of Mechanical and Aerospace Engineering Rutgers, The State University of New Jersey New Brunswick, New Jersey 08901*
Email: jiarong.chen@rutgers.edu
** *Email: qzzou@rutgers.edu*

Abstract: This paper presents an imaging mode of atomic force microscope (AFM) that is robust to the environmental acoustic noise. AFM operations are sensitive to external disturbances including acoustic noise, as disturbances to the probe-sample interaction directly results in distortions in the sample images obtained. Although conventionally passive noise cancellation has been employed, the passive-noise apparatus limits the function of AFM and its use in emerging applications. Moreover, residual noise still persists. In this work, we propose a noise rejection mode (NRM) of AFM imaging to avoid and eliminate the acoustic-caused disturbance to the imaging process. Contrary to other existing AFM imaging modes, in the proposed NRM approach, the set-point of the feedback loop for tracking the sample topography is adjusted online such that the AFM system is insensitive and thereby, robust to the environmental noise. Then, a feedforward controller is augmented to counter act the noise-caused vibration in the feedback loop. Both the set-point adjustment and the feedforward noise cancellation are implemented through finite-impulse-response (FIR) filters. Experimental examples are presented and discussed to illustrate the proposed technique.

Keywords: Active Noise Control, AFM Imaging, Finite Impulse Response.

1. INTRODUCTION

In this paper, a noise rejection mode (NRM) of atomic force microscope (AFM) imaging is proposed. As an essential tool for nanoscale interrogation and measurement, (Uchihashi et al. (2016a); Ren and Zou (2018); Uchihashi et al. (2016b)) AFM is sensitive to external and internal disturbances including acoustic noise, as disturbances to the tip-sample interaction directly result in the distortions in AFM images obtained (Gołek et al. (2014)). Although the adverse effects of external-disturbances can be alleviated via conventional passive methods (Ito et al. (2015); Benmouna and Johannsmann (2002)), residual noise distortion still persists. Thus, in this work we aim to develop the active control technique to combat the acoustic noise disturbances during the AFM imaging process.

Current AFM imaging modes are sensitive and thereby, not robust to external disturbances including acoustic noise. For example, contact-mode (CM) imaging (Eaton and West (2010)) is relatively simple, easy to implement, and fast (compared to other imaging modes). However, the sliding of the cantilever probe on the sample surface induces sample deformation and probe wear (Bloo et al. (1999); Saadi et al. (2020)), resulting in sample damage and image distortion. Such a sliding of the probe on the sample surface is largely eliminated through the development of the tapping-mode imaging (Hansma et al. (1994)), where, during the scanning, the probe "taps" on the sample surface near the resonance of the cantilever. Not only is the smear of the sample surface largely avoided, but also additional material properties can be acquired (Sundararajan and Bhushan (2002)). The TM-imaging has also been extended to the peak-force mode imaging (Hu et al. (2012)), with enhanced material property acquisition and imaging speed. In all these imaging modes, the set-point of the cantilever deflection is set at a pre-chosen constant, and any extraneous vibration of the probe is not accounted for, thereby, directly becoming distortions in the image obtained. Although much efforts have been made to eliminate these extraneous probe vibrations during AFM imaging, by improving the hardware bandwidth (Schitter et al. (2007)) or the control algorithms for the scanning (Kim and Zou (2008)) and sample topography tracking (Ren and Zou (2014a); Wu and Zou (2009)), the imaging speed improvement obtained is limited (Picco et al. (2006)) or accompanied with a substantial reduction of imaging size (Ando et al. (2013)). Contrary to all these work based on constant *fixed* set-point imaging modes, the set-point of cantilever deflection is online adaptively adjusted in the recently developed adaptive CM (Ren and Zou (2014a)) and adaptive multi-loop mode (Ren et al. (2014)), to substantially not only improve the imaging speed through an online data-driven iterative feedforward control, but also subdue the probe-sample interaction force through a gradient-based minimization process. The extraneous probe vibration is also accounted for in the image construction. All these existing AFM imaging modes, however, are sensitive to external ground vibration and environmental acoustic noise. Although traditionally, passive noise cancellation apparatus such as acoustic enclosures (Hansen (2003)) has been applied to isolate the environmental

10.1016/j.ifacol.2022.11.170

noise, the acoustic enclosures is bulky and expensive, limiting the use of AFM in critical applications such as the cleanroom in semiconductor industry and the integration of AFM with other instrument such as optical microscope with environment control chamber for live cell studies (Suzuki et al. (2013)). Therefore, techniques need to be developed to improve the robustness of the AFM imaging against environmental noise.

Challenges exist in active control of the acoustic-noise caused probe vibration. Unlike in conventional active noise cancellation applications, the acoustic-caused probe vibration during AFM operations cannot be eliminated by utilizing external acoustic source such as speaker to counter-act the environmental noise around the probe, (Gan et al. (2005); Tanaka and Tanaka (2010)) because the probe vibration is induced by the vibration modes of the mechanical structure of the AFM system to which the cantilever is mounted. Therefore, active control can only be applied through the piezoelectric actuation system of the cantilever. Moreover, the primary acoustic dynamics in AFM is complicated with no low-pass nature within the frequency range of interest. As a result, the counterpart of the acoustic-noise-caused vibration, is largely random, broadband, and does not decay obviously with frequency increasing. While the data-driven modeling of primary acoustic dynamics has been address in (Sicheng Yi (2018)), the error still exists in the model, causing residue distortion. Thus, for the active control technique to be effective, the complexity of the acoustic noise dynamics must be accounted for accurately.

The main contribution of this paper is the development of the NRM of AFM imaging that is robust to environmental acoustic noise. Specifically, the set-point of the cantilever deflection is online adjusted such that the feedback loop to track the sample topography is insensitive, i.e., robust, to the environmental acoustic noise. The online set-point adjustment is attained by passing the acoustic noise captured during the imaging process through a pre-filter. Then, an inversion-based feedforward controller is introduced to combat the noise-caused cantilever vibration. Finite-impulse-response (FIR)-based representation of the acoustic dynamics is utilized in the design of the controllers involved (Sicheng Yi (2018)). The proposed NRM-imaging technique is implemented in AFM imaging experiments, and the results show that the image distortion can be significantly reduced.

2. NOISE REJECTION IMAGING MODE

The proposed NRM-imaging is depicted in Fig. 1. Contrarily to conventional AFM imaging modes with a pre-chosen *fixed* set-point of the cantilever deflection (see A_{set} in Fig. 1), in the proposed NRM-imaging, the set-point of the cantilever deflection ($A_d[k]$ in Fig. 1) is online adjusted to account for the effect of the acoustic noise (n(k) in Fig. 1) on the AFM image obtained. Particularly, the set-point $A_d[k]$ is adjusted by using the measured acoustic noise signal n(k) via a pre-filter (see $G_d(z)$ in Fig. 1), such that the feedback controller to track the sample topography ($G_{FB}(z)$ in Fig. 1) won't "see" the acoustic-noise-caused cantilever vibration as sample topography tracking error. Thus, with this cantilever set-point adjustment, no extraneous acoustic-noise-caused piezoelectric actuator displacement is produced. As the sample topography image is generated by using the vertical z-axis displacement of the piezoelectric actuator that drives the cantilever to track the sample surface (Eaton and West (2010)), the acoustic-noise-caused distortion is avoided in the image.

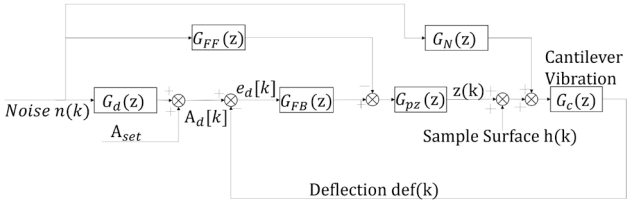

Fig. 1. Schematic block diagram of the proposed NRM of AFM imaging process in the presence of acoustic noise

With the above noise-rejection set-point adjustment, noise-induced cantilever vibration still exists albeit does not appear in the image obtained. Such an extraneous cantilever vibration, if large, can induce sample deformation (when the sample is soft) and deviation of the image obtained from the true sample topography. Thus, as in our previous work (Sicheng Yi (2018)), a feedforward control to counter-act the noise-caused cantilever vibration is augmented to the feedback loop ($G_{FF}(z)$ in Fig. 1).

2.1 Design of the Noise-Rejection Mode Imaging

Next we present the design of the controllers in the proposed NRM-imaging technique, i.e., design of the noise-rejection set-point filter $G_d(z)$ and the noise-rejection feedforward controller $G_{FF}(z)$. In the presence of the acoustic noise $n(z)$, the cantilever deflection during the imaging process is given by

$$\begin{aligned} d(z) &= S(z)[(-G_{FF}(z)G_s(z) + G_N(z))n(z) \\ &\quad + G_{FB}(z)G_s(z)A_d(z) + G_c(z)h(z)] \\ &= S(z)[G_{NC}(z)n(z) + G_{FB}(z)G_s(z)A_{set} \\ &\quad + G_c(z)h(z)] \end{aligned} \tag{1}$$

where $S(z)$ is the sensitivity of the feedback closed-loop,

$$S(z) = \frac{1}{1 + G_{FB}(z)G_s(z)} \tag{2}$$

$G_{NC}(z)$ is the dynamics from the noise to the cantilever deflection

$$\begin{aligned} G_{NC}(z) &= -G_{FF}(z)G_s(z) + G_N(z) \\ &\quad + G_{FB}(z)G_s(z)G_d(z) \end{aligned} \tag{3}$$

and $G_s(z) = G_{pz}(z)G_c(z)$ is the dynamics from the z-axis piezo actuator to the cantilever, respectively. In Eq. (3), $G_N(z)$ is the primary acoustic dynamics (PAD) from acoustic noise to the z-axis piezo movement.

The above Eq. (1) implies that to eliminate the acoustic noise effect on the cantilever deflection,

$$G_{FF}(z) = \hat{G}_N(z)G_s^{-1}(z) \tag{4}$$

where $\hat{G}_N(z)$ is a model of the PAD $G_N(z)$. PAD $G_N(z)$ is challenging to be captured and accounted for accurately—due to the complexity of the mechanical structure of AFM and the vibration of interests being at nanoscale. Thus, the feedforward controller can only be designed based on a

model of the PAD, $\hat{G}_N(z)$. Therefore, residual error exists with the feedforward controller,

$$E(z) := G_N(z) - \hat{G}_N(z) \neq 0 \tag{5}$$

Substituting Eqs. (4) and (5) into Eq. (1) yields

$$\begin{aligned} d(z) = S(z)[(E(z) + G_{FB}(z)G_s(z)G_d(z))n(z) \\ + G_{FB}(z)G_s(z)A_{set} + G_c(z)h(z)] \end{aligned} \tag{6}$$

The above Eq. (6) implies that by choosing the pre-filter of the set-point $G_d(z)$ as

$$G_d(z) = -E(z)G_{FB}^{-1}(z)G_s^{-1}(z) \tag{7}$$

the acoustic noise can be eliminated from the feedback loop and the feedback controller won't respond to the acoustic-noise-caused cantilever vibration. Thus, the set-point of the cantilever deflection is online adjusted for noise rejection as

$$A_d(z) = A_{set} - E(z)G_{FB}^{-1}(z)G_s^{-1}(z)n(z) \tag{8}$$

As such, the acoustic-noise-caused cantilever deflection is removed from the feedback error signal $e_d(k)$ (see Fig. 1), and the noise is rejected out of the feedback loop and the cantilever deflection becomes

$$d(z) = S(z)[G_{FB}(z)G_s(z)A_{set} + G_c(z)h(z)] \tag{9}$$

The above Eq. (9) shows that under the proposed NRM, the cantilever deflection only depends on the set-point A_set and the sample topography variation $h(z)$—the acoustic noise effect is eliminated.

2.2 Data-driven NRM-Imaging Control: Finite-Impulse-Response Approach

Key to the above NRM imaging approach is to characterize and quantify the dynamics of the acoustic dynamics involved, including the PAD $G_N(z)$, the dynamics from the z-axis piezo actuator to the cantilever deflection $G_s(z)$ (called the *piezo-to-cantilever* dynamics below), and the noise rejection filter $G_d(z)$. These frequency responses can be measured through AFM experiment (see Sec. 3 later for the detail). Then, instead of pursuing a parameterized-model-based approach, we propose to directly capture and quantify the acoustic dynamics via a finite-impulse-filter (FIR), for its efficacy and robustness in practical implementations (Sicheng Yi (2018)).

Specifically, the FIR representations of these three dynamics, $G_N(z)$, $G_d(z)$ and $G_s(z)$, are obtained by truncating the corresponding impulse responses measured in experiment to a finite series with a pre-chosen order as

$$G_N(z) \approx \hat{G}_{\mathrm{N}}(z) = \sum_{n=0}^{N_p-1} \omega_{n,k} z^{-k} \tag{10}$$

$$G_d(z) \approx \hat{G}_{\mathrm{d}}(z) = \sum_{n=0}^{N_d-1} \omega_{d,k} z^{-k} \tag{11}$$

$$G_s(z) \approx \hat{G}_{\mathrm{s}}(z) = \sum_{n=0}^{N_s-1} \omega_{s,k} z^{-k} \tag{12}$$

where $\omega_{\mathrm{n,k}}$,$\omega_{d,k}$ and $\omega_{s,k}$ are the coefficients of the impulse response of $\mathrm{G_N(z)}$, $G_d(z)$ and $G_s(z)$, respectively, and N_p, N_d *and* N_s are the corresponding orders chosen a priori, respectively. In practice, the FIR-filer coefficients $\omega_{n,k}s$ and $\omega_{s,k}s$ can be determined via a least-mean-square (LMS) minimization, e.g., $\omega_{n,k}s$ can be obtained via:

$$\min\left\{E(e_p^2(k))\right\} = \min\left\{E[(d(k) - \hat{d}(k)]^2\right\} \tag{13}$$

$$= \min\left\{E[(d(k) - \hat{g}_n(k) * n_p(k)]^2\right\} \tag{14}$$

where $d(k)$ and $\hat{d}(k)$ are the measured deflection and the estimated deflection, and $*$ denotes the convolution operation.

The above least-mean-squares minimization can be solved iteratively via:

$$\boldsymbol{\omega}_p(k) = \boldsymbol{\omega}_p(k-1) + 2\mu_p e_p(k)\boldsymbol{n}_p(k) \tag{15}$$

where

$$\boldsymbol{\omega}_p(k) = [\omega_{p,0}, \omega_{p,1}, ..., \omega_{p,k_{p-1}}]^T \tag{16}$$

is the vector of the iterative weights, and $\boldsymbol{n_p}(k)$ is the noise sequence measured. The iterative coefficients μ_p can be chosen experimentally to guarantee the convergence. The FIR coefficients $\omega_{s,k}$ and $\omega_{d,k}$ can be obtained similarly.

2.3 Sample Topography Estimation

Finally, we discuss the sample topography quantification that takes into account of the noise effect. Specifically, under the condition that the tip-sample contact is maintained throughout the imaging process (i.e., the tip-sample contact is in the repulsive region) and the sample deformation is negligible, then the sample surface topography is obtained by taking into account of the cantilever deflection variation as (Ren and Zou (2014b))

$$h_t(j) = z(j) + d_{ns}(j) - A_d(j) \tag{17}$$

$$= z(j) + d_{ns}(j) - d_n(j) - A_{set}, \quad j = 1, 2, \cdots, N_I \tag{18}$$

where $d_{ns}(j)$, $d_n(j)$ are the cantilever deflection measured during the imaging process under the acoustic noise effect, and the noise-caused cantilever deflection variation, N_I is the total number of sampling points over the entire image, respectively. Thus, compared to the previous sample topography quantification (Ren and Zou (2014b)) that only accounts for the deflection deviation (from the set-point value) caused by the error in tracking the sample topography, the noise-caused cantilever vibration is also accounted for. The noise-caused cantilever deflection $d_n(\cdot)$ cannot be measured directly during the imaging process. Thus, we proposed to estimate $d_n(\cdot)$ using the noise measured along the imaging process along with the FIR filter of $G_d(z)$ via

$$d_n(j) \approx n(j) * g_d(j) \tag{19}$$

3. EXPERIMENT IMPLEMENTATION

The proposed approach is demonstrated through AFM imaging experiments. The objective is to show that by using the proposed approach, the acoustic-caused image distortion can be substantially reduced.

3.1 Experimental Platform

The experiments were performed on a commercial AFM system (Dimension FastScan, BrukerNano Inc.) where direct access to all the sensing and actuating signals were provided, and the internal feedback control systems was bypassed when the external control signals were applied. The environmental acoustic noise with frequencies between 20 Hz and 1 kHz was induced by placing a speaker

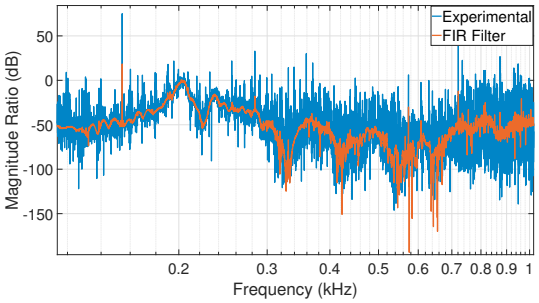

Fig. 2. Frequency response (magnitude part) of the measured primary acoustic dynamic and that estimated by using FIR filter, respectively.

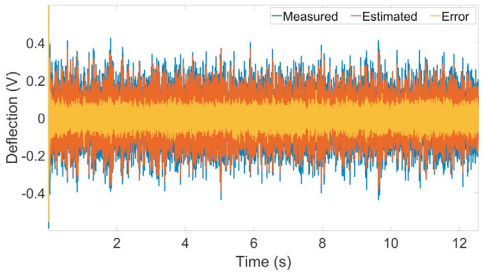

Fig. 3. Comparison of the FIR filter outputs to the measured outputs of z-axis displacements, along with the estimation error, respectively.

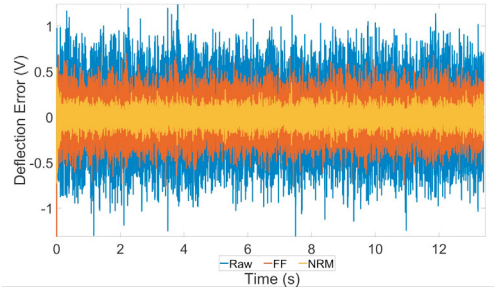

Fig. 4. Comparison of the deflection error $e_d[k]$ without active noise cancellation, with feedfoward controller, and with NRM-imaging technique, respectively.

(Logitech S150, Logitech, Inc.) near the AFM scanner head, and measured via a precision array microphone (BK 4958, Bruel Kjær Inc.). A homemade Op-Amp circuit was used to pre-filter and amplify the measured noise signal prior to acquisition through a Labview-FPGA system (NI RIO Device, USB-7856R, National Instrument Inc.). All the control algorithms were designed and implemented in Matlab. A Tapping-Mode(TM) cantilever (Model: FASTSCAN-C, Bruker Nano Inc.) was used and two types of samples, a silicon wafer and a cailbration sample (STR3-1800P, Bruker Inc.) were imaged. In the experiment, the sampling rate was set at 25 kHz, and the location of the acoustic noise source (the speaker) was treated unknown and thus, not used for the noise cancellation.

3.2 Experimental Implementation

To implement the proposed control scheme, we first identified and estimated the FIR-based model of PAD $G_N(z)$. Specifically, a proportional-integral(PI) feedback controller was designed and implemented as the vertical z-axis feedback loop (see Fig. 1) and the lateral x-y axis was also regulated at initial position via PI feedback control such that the cantilever stayed still and maintained the same deflection. Then, a band-limited (20-1kHz) white noise sound with zero-mean and standard deviation of 40 mV was applied to the environment through the speaker. Both the acoustic noise $\hat{n}[k]$ and deflection displacement of the piezo actuator $\hat{d}[k]$ were acquired when the acoustic noise was broadcasted for 1 second. The coefficients of the feedforward controller were identified online. The iteration coefficient was experimentally determined to minimize the measurement error.

Next, the obtained FIR feedforward controller was applied while the cantilever maintained still with noise broadcasted in the room. During this process the coefficients of noise rejection filter were determined using the same method as described in the above paragraph. Specifically, the residue deflection error $\hat{e}_d[k]$ was acquired while the feedforward controller was active and cantilever was stayed still. Hence, $A_d(z) = A_{set}$ and $H(z) = 0$ in Eq. (1), then the $G_d(z)$ are quantified as

$$G_d(z) = -E(z)G_{FB}^{-1}(z)G_s^{-1}(z) = \frac{\hat{e}_d(z)}{\hat{n}(z)} \qquad (20)$$

Finally, these two filters were applied to contact mode imaging of silicon sample and calibration sample. Both sample were imaged at a scan rate of 5 Hz. For comparison, images of these two samples were also acquired in the absence of the acoustic noise induced.

Results and Discussions

A 1024-order FIR model was chosen for the primary acoustic dynamic. The frequency response estimated by the FIR filter was compared to the corresponding experimentally measured ones in figure.2. To further validate the obtained FIR filters, we also compared the measured output with that of the corresponding FIR filter using a band-limited white noise input. (as shown in Fig. 3). The deflection fluctuation with respect to the set-point value (i.e., deflection error) obtained by using NRM technique is compared to those obtained by using the feedforward noise cancellation alone and by using PI-controller only in Fig. 4. Next, The AFM (height) images of the two samples under the acoustic noise applied is compared to those obtained by using the feedforward noise cancellation alone (Sicheng Yi (2018)) and those by using the proposed NRM-imaging technique, along with the acoustic-noise-free images in Fig. 5, respectively.

The preliminary results shown in Fig. 1-Fig. 4 demonstrated that the NRM mode can substantially reduced the deflection error compared to the chosen set-point which went into the PI controller. As shown in figure.2, the FIR filter captured the complicated primary acoustic noise dynamics well as most of the peaks and dips of the dynamics response were captured by the FIR filter. With the relative two-norm error less than 22%, the comparison shown in Fig. 3 also shows that by using the FIR filters obtained, the identified outputs followed the measured outputs closely. Thus, the experimental results showed that the obtained

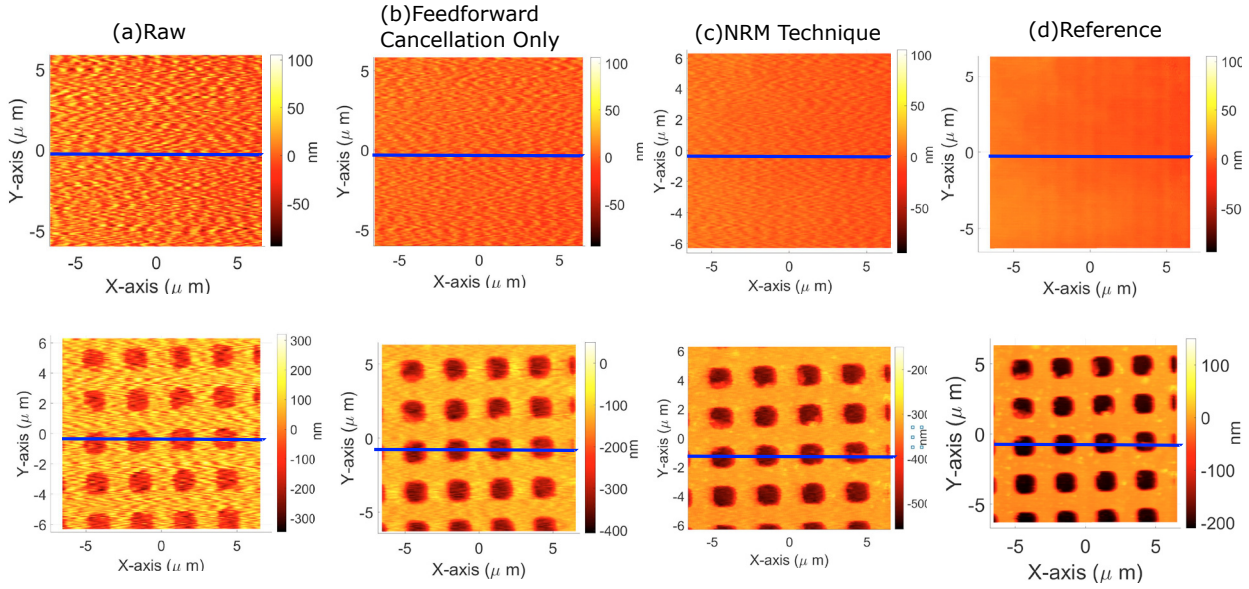

Fig. 5. Comparison of the topography image of the silicon sample (up) and the calibration sample (down) obtained (a) with the acoustic noise induced and without active noise cancellation, (b) with the induced acoustic noise and by using the feedforward control alone, (c) with the proposed NRM-imaging technique and (d) without the induced acoustic noise, respectively.

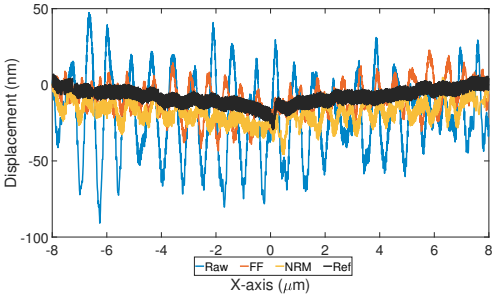

Fig. 6. Comparison of the cross-section topography profile of the silicon sample at the marked location in Fig. 4 for the four cases, respectively.

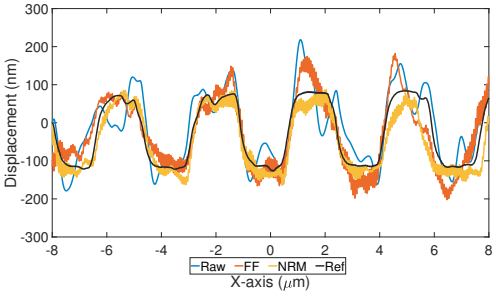

Fig. 7. Comparison of the cross-section topography profile of the calibration sample at the marked location in Fig. 4 for the four cases, respectively.

FIR filters captured the primary acoustic dynamics well. As a result, Fig. 4 demonstrated that the deflection error decreased by more than 50% when our technique was applied, proving that the feedforward controller and noise rejection filter did help with mitigating noise distortion and made the tracking more accurate.

The imaging results demonstrated that the distortion caused by acoustic noise can be substantially reduced by

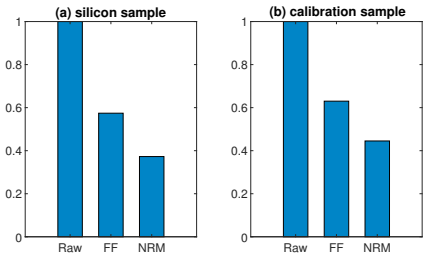

Fig. 8. Comparison of the normalized image error (with respect to the raw image error) for (a) the silicon sample and (b) the calibration sample in 2-norm, respectively.

using the proposed approach. It can be seen that the image quality of the topography obtained by using the FIR-based filtering technique compared well to that obtained in quiet environment (see Fig. 5 (c) and (d)). On the silicon sample, it was clear that the vibration distortions were reduced further with proposed technique (compare Fig. 5 (b) to (c)) on a very flat surface. While on calibration sample, both images presented clear image of the flat surface between the square-shaped pitches, whereas such areas were distorted in the images without active control (compare Fig. 5 (a) to Fig. 5 (b) and(c)). Meanwhile, the image of square pitches were not distinctively affected by acoustic noise. This difference can be seen more clearly in the cross section sample profile comparison in Fig. 6 to 7: the topography difference respect to the result obtained in quiet environment was 37% smaller when using the feedforward controller than that without our technique. And the high frequency oscillation introduced by the feedback controller was further reduced by around 55% when the noise rejection filter was applied on calibration sample and 63% on silicon sample. The normalized 2-norm error was shown in the bar figure Fig.8. Therefore, the experimental results

demonstrated the efficacy of the proposed approach.

4. CONCLUSION

In this article, a noise-rejection-mode (NRM) imaging was proposed to tackle acoustic-noise-caused cantilever probe vibration during AFM imaging. Specifically, the set-point of the feedback loop for topography tracking was adjusted online such that the AFM system was insensitive and robust to environment noise. A feedforward controller was augmented along the set-point pre-filter to counter act the the noise-caused vibration. The experimental results obtained under a band-limited white-noise induced to the environment demonstrated the efficacy of the proposed control method in tackling the acoustic-caused probe vibration during AFM imaging. By using the proposed technique, the image distortion was substantially reduced.

ACKNOWLEDGEMENTS

The financial support of NSF grants CMMI-1663055, CMMI-1851907 and IIBR-1952823 is gratefully acknowledged.

REFERENCES

Ando, T., Uchihashi, T., and Kodera, N. (2013). High-speed afm and applications to biomolecular systems. *Annual review of biophysics*, 42, 393–414.

Benmouna, F. and Johannsmann, D. (2002). Hydrodynamic interaction of afm cantilevers with solid walls: An investigation based on afm noise analysis. *The European Physical Journal E*, 9(1), 435–441.

Bloo, M., Haitjema, H., and Pril, W. (1999). Deformation and wear of pyramidal, silicon-nitride afm tips scanning micrometre-size features in contact mode. *Measurement*, 25(3), 203–211.

Eaton, P. and West, P. (2010). *Atomic force microscopy*. Oxford university press.

Gan, W.S., Mitra, S., and Kuo, S.M. (2005). Adaptive feedback active noise control headset: Implementation, evaluation and its extensions. *IEEE Transactions on Consumer Electronics*, 51(3), 975–982.

Gołek, F., Mazur, P., Ryszka, Z., and Zuber, S. (2014). Afm image artifacts. *Applied surface science*, 304, 11–19.

Hansen, C.H. (2003). *Solutions to Example Problems in Engineering Noise Control*. Causal Systems.

Hansma, P., Cleveland, J., Radmacher, M., Walters, D., Hillner, P., Bezanilla, M., Fritz, M., Vie, D., Hansma, H., Prater, C., et al. (1994). Tapping mode atomic force microscopy in liquids. *Applied Physics Letters*, 64(13), 1738–1740.

Hu, S., Mininni, L., Hu, Y., Erina, N., Kindt, J., and Su, C. (2012). High-speed atomic force microscopy and peak force tapping control. In *Metrology, Inspection, and Process Control for Microlithography XXVI*, volume 8324, 83241O. International Society for Optics and Photonics.

Ito, S., Neyer, D., Pirker, S., Steininger, J., and Schitter, G. (2015). Atomic force microscopy using voice coil actuators for vibration isolation. In *2015 IEEE International Conference on Advanced Intelligent Mechatronics (AIM)*, 470–475. IEEE.

Kim, K.S. and Zou, Q. (2008). Model-less inversion-based iterative control for output tracking: piezo actuator example. In *2008 American Control Conference*, 2710–2715. IEEE.

Picco, L.M., Bozec, L., Ulcinas, A., Engledew, D., Antognozzi, M., Horton, M., and Miles, M. (2006). Breaking the speed limit with atomic force microscopy. *Nanotechnology*, 18(4), 044030.

Ren, J. and Zou, Q. (2014a). High-speed adaptive contact-mode atomic force microscopy imaging with near-minimum-force. *Review of Scientific Instruments*, 85(7), 073706.

Ren, J. and Zou, Q. (2014b). High-speed adaptive contact-mode atomic force microscopy imaging with near-minimum-force. *Review of Scientific Instruments*, 85(7), 073706.

Ren, J. and Zou, Q. (2018). Adaptive-scanning, near-minimum-deformation atomic force microscope imaging of soft sample in liquid: Live mammalian cell example. *Ultramicroscopy*, 186, 150–157.

Ren, J., Zou, Q., Li, B., and Lin, Z. (2014). High-speed atomic force microscope imaging: Adaptive multiloop mode. *Physical Review E*, 90(1), 012405.

Saadi, M.A.S.R., Uluutku, B., Parvini, C.H., and Solares, S.D. (2020). Soft sample deformation, damage and induced electromechanical property changes in contact- and tapping-mode atomic force microscopy. *Surface Topography: Metrology and Properties*, 8(4), 045004. doi:10.1088/2051-672x/abb888. URL `https://doi.org/10.1088/2051-672x/abb888`.

Schitter, G., Astrom, K.J., DeMartini, B.E., Thurner, P.J., Turner, K.L., and Hansma, P.K. (2007). Design and modeling of a high-speed afm-scanner. *IEEE Transactions on Control Systems Technology*, 15(5), 906–915.

Sicheng Yi, Tianwei Li, Q.Z. (2018). Active control of acoustics-caused nano-vibration in atomic force microscope imaging. *Ultramicroscopy*, 195, 101–110.

Sundararajan, S. and Bhushan, B. (2002). Development of afm-based techniques to measure mechanical properties of nanoscale structures. *Sensors and actuators A: Physical*, 101(3), 338–351.

Suzuki, Y., Sakai, N., Yoshida, A., Uekusa, Y., Yagi, A., Imaoka, Y., Ito, S., Karaki, K., and Takeyasu, K. (2013). High-speed atomic force microscopy combined with inverted optical microscopy for studying cellular events. *Scientific reports*, 3(1), 1–7.

Tanaka, N. and Tanaka, M. (2010). Active noise control using a steerable parametric array loudspeaker. *The journal of the acoustical society of America*, 127(6), 3526–3537.

Uchihashi, T., Watanabe, H., Fukuda, S., Shibata, M., and Ando, T. (2016a). Functional extension of high-speed afm for wider biological applications. *Ultramicroscopy*, 160, 182–196.

Uchihashi, T., Watanabe, H., Fukuda, S., Shibata, M., and Ando, T. (2016b). Functional extension of high-speed afm for wider biological applications. *Ultramicroscopy*, 160, 182–196.

Wu, Y. and Zou, Q. (2009). An Iterative-Based Feedforward-Feedback Control Approach to High-Speed Atomic Force Microscope Imaging. *Journal of Dynamic Systems, Measurement, and Control*, 131(6).